Shear heating during rapid subduction initiation beneath the Samail Ophiolite

Joshua M. Garber[1,*]
Matthew Rioux[2]
Andrew J. Smye[1]
Alicia M. Cruz-Uribe[3]
Peter L. Baker[4]
Jeffrey D. Vervoort[4]
Michael P. Searle[5]
Maureen D. Feineman[1]

[1]The Pennsylvania State University
[2]University of California, Santa Barbara
[3]University of Maine
[4]Washington State University
[5]Oxford University
*corresponding author: jxg1395@psu.edu

[This version of the article has been accepted for publication, after peer review, and is subject to Springer Nature's Accepted Manuscript terms of use, but is not the Version of Record and does not reflect post-acceptance improvements, or any corrections. The Version of Record is available online at: https://doi.org/10.1038/s41561-025-01711-6]

Metamorphic soles beneath ophiolites are thought to record subduction initiation. However, there is ambiguity about the tectonic and thermal mechanisms operative during subduction initiation, arising partly from uncertainty in the duration of sole metamorphism. Here, we use chemical mapping and diffusion speedometry of garnet crystals from the metamorphic sole of the Samail Ophiolite (Oman/United Arab Emirates) to show that high-temperature (≥750°C) metamorphism was rapid, lasting ≤1 Myr (potentially ≤100 kyr) at peak temperature conditions. The short durations are supported by zircon U-Pb ages and new garnet-whole rock-zircon Lu-Hf data from the same rocks, contrasting with previous inferences for ≥8 Myr metamorphic durations. These observations are nominally consistent with the spontaneous sinking of a dense lower plate. However, the rapid metamorphic timescales cannot be accounted for solely by conductive thermal equilibration with juxtaposed oceanic mantle. One potential explanation is dissipative heating driven by relative motion across the nascent plate interface. This interpretation accounts for the timescales, spatial pattern of metamorphism, and the global similarities in sole pressure-temperature conditions independent of other geodynamic variables.

Ophiolites are obducted pieces of oceanic crust and mantle connecting two plate tectonic themes: oceanic crust formation at mid-ocean ridges and its consumption at subduction zones. Metamorphic soles welded beneath many ophiolites are integral to this connection, as they likely represent the first-preserved remnants of a nascent subducted slab formed during subduction initiation (SI)[1, 2]. Ophiolite-sole relationships can be used to test the geodynamic configurations that foster SI, and whether it was spontaneous (driven by gravitational sinking of a dense slab) or induced (by horizontal tectonic forces) [3-5]. These data can also be used to quantify boundary conditions favorable for SI throughout Earth history[6-9].

However, the thermal evolution of sole metamorphism remains controversial. For even the best-exposed ophiolites, diverse geochronological methods have yielded disparate potential sole metamorphic durations. The most complete sole exposures have inverted metamorphic temperature (*T*) gradients from granulite (800-900°C) to greenschist facies (<500°C) over ~100s of m, stepping structurally downward from their overlying ophiolites[10, 11]. In the archetypal Samail Ophiolite (Oman/United Arab Emirates [UAE]) (**Fig. 1a**), Earth's largest example of obducted oceanic lithosphere, coupled uranium-lead (U-Pb) dates and trace elements in zircon from the hottest, topmost sole rocks suggest a short phase of granulite-facies sole metamorphism, occurring at most ≤500 ka prior to the magmatic crystallization of the ophiolite crust (96.70±0.09–95.16±0.06 Ma sole zircon ages *vs.* 96.13±0.05–95.24±0.03 Ma ophiolite zircon ages) [12-16]. This rapid interval matches the short SI timescales inferred from the analogous Izu-Bonin-Mariana forearc system[17, 18], thought to have formed by spontaneous slab sinking[9, 19]. In contrast, ~104 Ma garnet-whole rock lutetium-hafnium (Lu-Hf) isochron dates for the same sole granulites suggest that a lengthy period of high-*T* sole metamorphism occurred during tectonically induced thrusting ~8 Myr prior to ophiolite formation, followed by ~96 Ma zircon crystallization during cooling as subduction became self-sustaining[3].

These and other datasets[20, 21] support potential durations of sole heating spanning an order of magnitude (~1–10 Myr), precluding a rigorous understanding of SI in the archetypal Samail system. The age uncertainty further propagates to ambiguity in the thermal mechanism(s) for sole heating, including whether conductive heating from the overlying ophiolite is solely responsible for high-*T* sole metamorphism[5, 6]. Crucially, similar tectonic and thermal ambiguities are present in other ophiolite-sole couples worldwide.

Precise temperature-time (*T-t*) histories to rigorously test these timescales can be accessed by multiple methods. Here, we chemically mapped metamorphic garnet in the highest-grade Samail sole rocks, and modeled the diffusive relaxation of major- and trace-element discontinuities to constrain their duration at peak *T*. These data are supplemented by new Lu-Hf and previously published U-Pb geochronology from the same samples. Together, these data reveal internally consistent diffusion and dating timescales, which are used to understand the integrated sole *T-t* history and physical mechanisms for sole heating.

Metamorphic sole textures and chemical zoning

We focused on two southern Samail outcrops: Wadi Tayin and Hammah Window[14, 22, 23] (**Fig. 1a**). These sole exposures exhibit a topmost ≤5 m layer of garnet- and clinopyroxene-bearing (grt-cpx) mafic amphibolites (peak pressure-temperature [*P-T*] conditions = ~10–15 kbar, 750–900°C) overlain by ophiolitic mantle harzburgite along the Samail Thrust[24], grading to amphibolite-facies (*T*~500°C) mafic and metasedimentary rocks at their base over ≥100 m structural thickness[2, 10, 22, 25-28]. Notably, these southernmost Samail soles have thinner garnet-bearing horizons than those in northern Oman and the UAE (≥30 m) [10, 27], and record the youngest Samail sole radiometric dates[12, 14, 23].

Two grt-cpx amphibolite samples collected <1 m from the Samail Thrust underwent detailed analysis: 13OJG**WT15** (Wadi Tayin; 23.0621°N/58.6021°E) and 171213**J02** (Hammah; 23.1006°N/58.5358°E). Each sample contains ≤0.5 cm garnet poikiloblasts set in a matrix of finer-grained clinopyroxene, hornblende, ilmenite, titanite, and variably altered plagioclase (**Fig.

1b). Though their matrices are mostly retrogressed[29], rare subhedral garnet crystals exhibit inclusion assemblages consistent with prograde garnet crystallization. In **WT15**, pink garnet cores and mantles include amphibolite-facies (green amphibole + plagioclase + titanite) to granulite-facies mineral assemblages (clinopyroxene + brown amphibole + plagioclase + ilmenite + apatite), with pale, inclusion-free rims (**Fig. 1b; Fig. S1**). In **J02**, rare inclusion-free garnet cores transition to garnet rims with globular, granulite-facies inclusions (clinopyroxene + brown amphibole + ilmenite + apatite) (**Fig. 1c**). Other garnet crystals in both samples occur as anhedral aggregates with clinopyroxene, ilmenite, and subsidiary hornblende (**Fig. S2**), consistent with solely granulite-facies (re)crystallization.

Garnet chemical maps reveal several generations of chemical zoning. In **WT15**, abrupt major-element discontinuities (≤200 μm-width) separate granulite-facies mantles and rims from amphibolite-facies garnet cores, with flat zoning on either side (**Fig. 2b**). Such textures indicate partial resorption or recrystallization along the heating path. Trace-element zoning shows no evidence of this resorption boundary, and instead is dominated by crystal growth features. Rare-earth elements (REE) exhibit concentric changes from core to inner rim, with oscillatory zoning at garnet rims. Sharp compositional boundaries (≤40 μm-width) are observed within and between amphibolite and granulite-facies zones, particularly in Lu (**Fig. 2c**). Chromium maps reveal broadly similar zoning patterns, albeit with inherited low-Cr relics in garnet cores and local alteration haloes around inclusions in garnet mantles (**Fig. 2d**).

Hammah sample **J02** shows similar but less complex zoning. Garnet major-element profiles exhibit a ~200–400 μm-wide Mg and Mn shift correlating with the first occurrence of granulite-facies inclusions at garnet rims (**Fig. 2e-2f**). This mineralogic and major-element change further coincides with a transition from long-wavelength concentric REE zoning in garnet cores to short-wavelength oscillatory zoning in garnet rims (**Fig. 2g**), including similar low-Cr relics (**Fig. 2h**).

Major and trace element diffusion speedometry

The major and trace-element zoning suggest punctuated garnet crystallization and partial resorption during prograde heating, with incomplete diffusive relaxation of sharp compositional gradients during and after peak conditions. Modelling the *T-t* histories permitted by these discontinuities first requires accurate constraints on peak metamorphic temperatures. Prior thermobarometry[10, 22, 30] suggests ~750–850°C peak temperatures; we supplemented these constraints with new garnet-clinopyroxene Fe-Mg[31, 32] and REE thermobarometry[33], as well as published Ti-in-zircon temperatures[14]. The Fe-Mg and Ti-in-zircon results (**Fig. S3**) indicate ~750–800°C peak temperatures for both samples, with some data extending to hotter conditions (~800–850°C). REE thermobarometry yielded ~900°C peak temperatures for both samples, but we consider these suspect due to systematic offsets in Samail garnet major-element compositions relative to those in the REE calibration experiments[33, 34]. We therefore adopted the ~750–800°C Fe-Mg and Ti-in-zircon results as minimum peak temperatures.

We determined peak-*T* timescales by inverting stranded diffusion profiles within individual garnet crystals, using one-dimensional numerical (major elements[35]) and analytical (Lu[36]) approaches. We tested several published diffusion parameters for major[37-40] and trace elements[41-43] in garnet, with variable peak temperatures (~700–800°C) (**Fig. S4-S5**). Calculations were initially performed for isothermal diffusion to provide a maximum possible duration above peak temperature. Each elemental profile uniquely determines the time-integrated magnitude of intracrystalline volume diffusion, <*Dt*> (m^2), which captures the total amount of diffusionfacilitated mass transport. For major elements, the sharpest, <200 μm chemical discontinuities developed at peak *T* in sample **WT15** (**Fig. 2a-b**) cannot have been maintained for more than ~100 kyr at ≥750°C (**Fig. 3**; **Fig. S4**). The wider major-element discontinuity (≤400 μm) co-located with the first appearance of granulite-facies inclusions in sample **J02** (**Fig. 2f**) is likewise consistent with ~100-200 kyr at peak *T*. For Lu, the range and uncertainty of possible diffusion parameters[41-43] yield order-of-magnitude differences in calculated timescales, and thus represent general bounds on the maximum duration at peak *T*. We modeled three of the sharpest garnet Lu profiles, as these most plausibly represent step-function starting conditions: one from the amphibolite-facies **WT15** core; one from the oscillatory-zoned, inclusion-free rim of the same **WT15** garnet; and one from the oscillatory-zoned, granulite-facies **J02** rim (**Fig. 4**; **Fig. S5**).

For the **WT15** garnet core (**Fig. 4a**), maximum Lu diffusive timescales at ~750°C are ~1 Myr (**Fig. 4d**); for the **WT15** rim (**Fig. 4b**), these calculations suggest a maximum of ~200 kyr of diffusion at ~750°C (**Fig. 4e**). The **J02** rim profile (**Fig. 4c**) shows intermediate diffusive timescales (**Fig. 4f**). Together, these models demonstrate that – unless peak temperatures have been grossly overestimated – it is unlikely that the Samail sole rocks experienced peak conditions (≥750°C) for >1 Myr. Additionally, these calculated timescales are maxima because **i**) assuming an initial step function maximizes $<Dt>$[44]; **ii**) off-center sampling transects would artificially elongate concentration profiles; **iii**) peak temperatures could have been hotter (≤900°C); and **iv**) our isothermal modelling ignores diffusion during heating to and cooling from the thermal climax. Accordingly, the duration of each sample at peak *T* could have been as short as ≤100 kyr. Finally, though there are myriad possible origins of oscillatory REE zoning in garnet[45] – e.g., fluctuations in fluid activity, temperature, growth rate, or dissolution – no existing evidence suggests that such zoning diffusively relaxes differently than other zoning types, and the short diffusive timescales are recovered from both oscillatory and non-oscillatory zoned garnet portions (**Figs. 3-4**).

Isotopic dating of sole metamorphism

The garnet diffusion timescales match zircon U-Pb timescales from the same rocks: prograde (650–800°C) garnet growth recorded by zircon in **WT15** and **J02** occurred over 0.47±0.15 Myr (95.95±0.06–95.48±0.09 Ma) and 0.28±0.15 Myr (96.08±0.07–95.80±0.09 Ma), respectively[14] (**Fig. 5c**). However, the garnet diffusion and zircon U-Pb timescales are far shorter than those from published Samail sole garnet-WR Lu-Hf isochron dates, which yield older dates for garnet growth (104 Ma[3]), implying ≥8 Myr at peak *T*. To directly compare U-Pb, Lu-Hf, and diffusion timescales in a single sample, we determined a garnet-WR Lu-Hf isochron date for **J02**. Four garnet and two whole-rock aliquots from **J02** yield a Lu-Hf isochron date of 98.1±1.3 Ma (mean squared weighted deviation [MSWD] = 4.6) (**Table S1**). Previously published LA-MC-ICPMS Lu-Hf data from the ~96.1–95.8 Ma zircons in the same rock[14] lie near the isochron intercept (**Fig. 5b**). Including all zircon data (n=20) with the garnet and WR data yields the same Lu-Hf isochron age within uncertainty (97.9±0.5 Ma) and a smaller MSWD (1.6) (**Fig. 5a**); including one weighted-mean zircon Lu-Hf datum yields an intermediate isochron date (98.0±1.1 Ma) and MSWD (3.8). Importantly, the **J02** isochron exhibits higher garnet ^{176}Lu/^{177}Hf ratios and a higher initial Hf ratio (ε_{Hf} = +12.6) than the previously published ~104 Ma garnet-WR Lu-Hf isochrons[3] (ε_{Hf} = -5 to -12) (**Fig. 5a**). These latter ε_{Hf} intercepts are significantly lower than other published ε_{Hf} data from the Samail metamorphic sole metabasalts[14] (ε_{Hf} = +4.5 to +14.6, excluding inherited zircon from a single sample). If accurate, the previously published Lu-Hf dates must have been sourced from rocks not represented in other Samail sole sample suites, even from the same outcrops; alternatively, such spurious intercepts signify that the calculated ages are inaccurate.

Though our new Lu-Hf isochron date (97.9±0.5 Ma) is slightly older than the zircon U-Pb dates from the same sample (96.08±0.07–95.80±0.09 Ma), this ~2 Myr offset does not necessarily represent a geologically significant garnet growth duration. Fully propagated uncertainties on U-Pb and Lu-Hf dates (**Text S1**) yield a minimum ~500-800 kyr between them, consistent with the diffusion speedometry. Other data additionally require zircon and garnet co-crystallization: zircon inclusions occur in garnet, and zircon trace-element data record evolving garnet-absent (Yb/Dy>5) to garnet-present (Yb/Dy<5) conditions over ~200–400 kyr (**Fig. 5c**) [14]. Further, zircon-bearing and zircon-free Lu-Hf isochrons for **J02** each independently yield the same initial ε_{Hf} (**Table S1**), demonstrating rock-wide Hf isotopic equilibrium. The most permissible constraints on garnet growth durations (including but not limited to granulite-facies conditions) are therefore ~2 Myr, but we suggest that the ≤1 Myr durations determined independently from each dataset are more readily supported, and either case firmly excludes ≥8 Myr durations at granulite-facies conditions. Finally, titanite and monazite U-Pb geochronology measured by laser-ablation inductively coupled plasma mass spectrometry (LA-ICPMS) has also been used to argue for ~5–10 Myr metamorphic durations in the Samail sole[20], but these reported ages are highly sensitive to data reduction parameters, and the underlying data are equally consistent with the shorter durations found here (**Text S2, Fig. S12**). In contrast, our multi-mineral and multi-method approach firmly connects the timing of sole metamorphism and the magmatic crystallization of the ophiolite crust (96.13±0.05–95.24±0.03 Ma).

Thermal and tectonic implications

The new and existing *T-t* data place strict bounds on the thermal and tectonic mechanisms responsible for Samail metamorphic sole formation:

1. Prograde heating (~650–800°C) was ≤500 kyr at the studied outcrops[14].
2. The total duration of ≥750°C metamorphism was ≤1 Myr (this study).
3. Amphibolite-facies metamorphism (~700–500°C) of the entire sole section occurred ≤1.5 Myr after peak temperatures were attained in the highest-grade, garnet-bearing rocks[14, 25]. It is unclear whether the topmost rocks were exhumed as they experienced these cooler temperatures; some studies have estimated ~1–3 kbar of exhumation during early retrogression[10, 25], but several studies have shown the grt-cpx granulites probably remained at similar depths as they initially cooled[27, 46].
4. Sole protoliths were >100 Ma at the time of sole formation[2].
5. The preserved granulite-facies sole interval at Wadi Tayin and Hammah Window rarely exceeds ~5 m in thickness[10, 22, 26]. This layer must have been somewhat attenuated, but the absolute amount of thinning is difficult to quantify. Minimum sole shear strains have been estimated at γ~5 based on amphibolite textures[10, 29] (i.e., a thinning factor of 4).
6. Tonalitic melts cross-cut the garnet-clinopyroxene metabasalts, but these were added from underlying, lower-grade metabasalts and metasediments[12, 14]. In contrast, the grt-cpx rocks demonstrably lost melt at suprasolidus conditions[10].

Combined with our diffusion speedometry, these constraints define permissible *T-t* histories, providing insights into heat transfer mechanisms during nascent subduction. **Figure 6** shows two thermal histories that account for the total integrated *T-t* path, and satisfy the Lu elemental profiles preserved in garnet core ($\log_{10}\langle D_{Lu}t\rangle=-9.96$) and rim domains ($\log_{10}\langle D_{Lu}t\rangle=-10.62$). Independent of the operative garnet Lu diffusion mechanism, the calculated heating and cooling timescales are ~10^5 years – implicating some of the shortest-duration granulite-facies assemblages yet reported from the rock record. While these thermal histories are not precisely determined, the exponential thermal dependence of diffusion rates, in concert with the additional geochronology and major-element speedometry, rends vastly different thermal histories as implausible.

Contemporaneous Samail sole metamorphism and ophiolite magmatic crystallization nominally implicates spontaneous SI[17-19], in which a cooler, denser lower plate sinks into the mantle beneath a hotter, thinner, younger upper plate, causing asthenospheric upwelling that conductively heats the slab-mantle interface[5, 6, 9]. However, purely conductive heating contrasts with the exceptionally brief high-*T* temperatures and cooling, as well as the short length-scales of sole metamorphism. To investigate heating mechanisms and subduction/exhumation rates that satisfy the *P-T-t* and length-scale constraints, we constructed a 2-D thermal-kinematic model of the nascent Samail subduction interface (**Text S3; Fig. S14**). Our calculation demonstrates that thrusting a ~150 Ma slab beneath a ~2 Ma oceanic upper plate should result in peak *P-T* conditions matching those in the Samail sole, but with conductive heat transfer into the slab over ~5–11 km distances given the requisite convergence velocities (2–4 cm/yr). Even considering reasonable attenuation magnitudes, such length scales far exceed those observed for granulite-facies sole metamorphism at the studied outcrops (~5 m). Further, the observed rapid high-*T* cooling (100–200 °C/Myr at $T>600$°C) would require plate-rate exhumation (1–2 cm/yr), which is unlikely given the lack of significant exhumation during initial cooling[27, 46] and the limited buoyancy of the garnet amphibolites[12].

We contend that the rapid heating, cooling, and meter-scale metamorphic aureole indicate a transient heat source along the slab-top interface during the highest-*T* portion of nascent subduction. Frictional or viscous heat dissipation driven by relative motion across the slab-mantle interface addresses numerous observations that cannot be satisfied by other models. Like those in Oman, thermal gradients on the order of ~100°C/km are expected to develop perpendicular to the subduction interface during shear heating[47]. As heat generation is inextricably linked to deformation, migration of the primary deformation plane (or planar interval) during subduction would account for the generation of cross-cutting tonalitic melts from underlying metabasalts and metasediments[12, 14] as well as the rapid cooling rates. Estimates of the potential contribution of dissipative heating to sole metamorphism can be obtained from a scaling analysis[48] (**Text S3; Fig. S15**): for a ~1–10 m thick shear zone at 30 km depth, an initial temperature of 600°C, 2-4 cm/yr convergence velocities, and rock viscosities ~10^{20} Pa-s, the shear heating fractional contribution to the thermal budget of the shear zone varies from 30-90%. These results demonstrate that shear heating could have contributed a significant portion of heat along the high-*T* portion of the metamorphic path. Further, the migration of the principal shear zone from above to below sole rocks provides a parsimonious explanation for the rapid cooling rates required at T>600°C (**Fig. 6**), as such cooling would occur at a constant depth[47].

The role of shear heating in metamorphic soles could help explain why soles globally exhibit similar high-*T* conditions in their topmost portions even with highly variable lower and upper plate ages at the time of SI[1, 49], which should have a measurable effect on their resulting *P-T* conditions. Such transient, deformation-related effects would also explain why *P-T* conditions of metamorphic soles deviate so significantly from any long-term subduction thermal field. Future work should perform similar high-resolution *P-T-t* work to quantify how much of the sole thermal structure during SI is preserved during the transition to mature subduction.

ACKNOWLEDGEMENTS

We thank the Director General of Minerals, Ministry of Commerce and Industry of the Sultanate of Oman for allowing us to conduct field work in the Sultanate of Oman. K. Crispin is thanked for EPMA assistance; A. Nikitin is thanked for assistance with 171213J02 Lu-Hf sample preparation; J. Cottle, A. Kylander-Clark, T. Mittal, R. Parrish, and J. Wakabayashi are thanked for discussions regarding the manuscript. This research was supported by National Science Foundation grant EAR-2120931 to JMG and AJS, National Science Foundation grants EAR-1250522 and EAR-1650407 to MR, and The Pennsylvania State University

Author Contributions

JMG, MR, and AJS conceived the study. JMG and MR carried out sample collection and preparation. JMG performed petrographic analysis, LA-ICPMS spot analyses, major-element and REE thermometry, Lu diffusion speedometry, and supervised EPMA mapping; AC and JMG performed LA-ICPMS mapping; PB and JV performed Lu-Hf isotopic data collection; MDF performed quantitative EPMA spot transects; and AJS performed the garnet major-element diffusion speedometry and thermal-kinematic modelling. JMG wrote the original manuscript; all authors contributed to final data interpretation and manuscript writing.

Competing Interests Statement

The authors declare no competing interests relevant to this study.

Figure Captions

Figure 1: Geological map and sample textures. A) Tectonic sketch map of the Samail Ophiolite divided into crustal, mantle, and metamorphic sole; sample locations for this study are marked by the yellow-outlined orange star. Figure modified from ref. [14]. **B**)-**C**) Garnet crystals from samples 13OJG**WT15** (Wadi Tayin; **B**) and 171213**J02** (Hammah; **C**) that exhibit prograde-to-peak mineralogical and chemical zoning. The locations of chemical maps in Fig. 2 are outlined in black (EPMA) and white (LA-ICPMS).

Figure 2: Garnet chemical maps and transect locations. Electron-probe microanalysis (EPMA) X-ray maps of Mg (**A, E**) and Mn (**B, F**), and laser-ablation inductively coupled plasma mass spectrometry (LA-ICPMS) maps of Lu (**C, G**) and Cr (**D, H**) for the garnets shown in Fig. 1b-c. Chemical transects that were modeled for diffusive relaxation timescales (**Figs. 3-4**) are shown as white lines.

Figure 3: Garnet major-element speedometry. Major-element data ($\pm 2\sigma$) from sample WT15 used for diffusion modelling (top) with an accompanying diffusion speedometry model based on the diffusion parameters from ref. [37] (bottom). See Methods for additional details, as well as **Figure S4** for models based on other literature diffusion parameters.

Figure 4: Garnet Lu diffusion speedometry. Garnet trace-element transects (**A-C**) and diffusion speedometry model calculations (**D-F**) for the profiles shown graphically in Fig. 2. These calculations were performed using the online version of the Diffuser software[36], for three

different sets of experimentally measured diffusion parameters, and assuming isothermal, peak-*T* conditions. Lu error bars in all panels are two standard errors of the mean (2SE).

Figure 5: Lu-Hf and U-Pb isotopic data. A) New solution Lu-Hf isotopic data from Hammah sample 171213**J02** (red = garnet, blue = whole-rock), previously published zircon LA-ICPMS Lu-Hf data from the same sample (yellow) [14], and previously published solution Lu-Hf data from Guilmette et al. [3] (gray). Errors (±2σ) are smaller than symbols for all data. **B**) Zoomed-in view of previously published zircon Lu-Hf isotopic data (±2σ) from sample **J02**[14]. Brown zircon data have elevated HREE consistent with zircon growth prior to or synchronously with garnet, whereas yellow data have lower HREE consistent with growth during or after garnet crystallization. Two isochrons including the garnet and whole-rock data (near-horizontal due to expanded scale) are shown for reference, one (black) including the zircon data and the other (gray) excluding these data; note that even the zircon-free isochron passes through the zircon data. **C**) TIMS U-Pb isotopic data (±2σ) from the same zircons shown in (B)[14].

Figure 6: Thermal histories of the Samail sole. Two possible *T-t* trajectories for the uppermost Samail sole at Wadi Tayin and Hammah, using the integrated sum of Lu diffusion in garnet (profiles in Fig. 4d-f), accounting for both heating and cooling paths, assuming either the fastest (blue) or slowest (red) possible Lu diffusion mechanisms in garnet[41], and incorporating other relevant *T-t* data (as discussed in the main text).

REFERENCES

1. Agard P, Yamato P, Soret M, Prigent C, Guillot S, Plunder A*, et al.* Plate interface rheological switches during subduction infancy: Control on slab penetration and metamorphic sole formation. *Earth and Planetary Science Letters* 2016, **451:** 208-220.

2. Searle MP, Cox J. Subduction zone metamorphism during formation and emplacement of the Semail ophiolite in the Oman Mountains. *Geological Magazine* 2002, **139**(3)**:** 241-255.

3. Guilmette C, Smit MA, van Hinsbergen DJJ, Gürer D, Corfu F, Charette B*, et al.* Forced subduction initiation recorded in the sole and crust of the Semail Ophiolite of Oman. *Nature Geoscience* 2018, **11**(9)**:** 688-695.

4. Lallemand S, Arcay D. Subduction initiation from the earliest stages to self-sustained subduction: Insights from the analysis of 70 Cenozoic sites. *Earth-Science Reviews* 2021, **221:** 103779.

5. Zhou X, Wada I. Differentiating induced versus spontaneous subduction initiation using thermomechanical models and metamorphic soles. *Nature Communications* 2021, **12**(1)**:** 4632.

6. Duretz T, Agard P, Yamato P, Ducassou C, Burov EB, Gerya TV. Thermo-mechanical modeling of the obduction process based on the Oman Ophiolite case. *Gondwana Research* 2016, **32**(Supplement C)**:** 1-10.

7. Gurnis M, Hall C, Lavier L. Evolving force balance during incipient subduction. *Geochemistry, Geophysics, Geosystems* 2004, **5**(7)**:** n/a-n/a.

8. Leng W, Gurnis M. Dynamics of subduction initiation with different evolutionary pathways. *Geochemistry, Geophysics, Geosystems* 2011, **12**(12).

9. Maunder B, Prytulak J, Goes S, Reagan M. Rapid subduction initiation and magmatism in the Western Pacific driven by internal vertical forces. *Nature Communications* 2020, **11**(1)**:** 1874.

10. Soret M, Agard P, Dubacq B, Plunder A, Yamato P. Petrological evidence for stepwise accretion of metamorphic soles during subduction infancy (Semail ophiolite, Oman and UAE). *Journal of Metamorphic Geology* 2017.

11. Dewey JF, Casey JF. The sole of an ophiolite: the Ordovician Bay of Islands Complex, Newfoundland. *Journal of the Geological Society* 2013, **170**(5)**:** 715-722.

12. Rioux M, Garber J, Bauer A, Bowring S, Searle M, Kelemen P, Hacker B. Synchronous formation of the metamorphic sole and igneous crust of the Semail ophiolite: New constraints on the tectonic evolution during ophiolite formation from high-precision U–Pb zircon geochronology. *Earth and Planetary Science Letters* 2016, **451:** 185-195.

13. Rioux M, Garber JM, Searle M, Kelemen P, Miyashita S, Adachi Y, Bowring S. High-Precision U-Pb Zircon Dating of Late Magmatism in the Samail Ophiolite: A Record of Subduction Initiation. *Journal of Geophysical Research: Solid Earth* 2021, **126**(5)**:** e2020JB020758.

14. Rioux M, Garber JM, Searle M, Crowley JL, Stevens S, Schmitz M*, et al.* The temporal evolution of subduction initiation in the Samail ophiolite: High-precision U-Pb zircon

petrochronology of the metamorphic sole. *Journal of Metamorphic Geology* 2023, **n/a**(n/a).

15. Rioux M, Bowring SA, Kelemen PB, Gordon S, Dudás F, Miller R. Rapid crustal accretion and magma assimilation in the Oman-U.A.E. ophiolite: High precision U-Pb zircon geochronology of the gabbroic crust. *Journal of Geophysical Research* 2012, **117**.

16. Rioux M, Bowring S, Kelemen P, Gordon S, Miller R, Dudás F. Tectonic development of the Samail ophiolite: High-precision U-Pb zircon geochronology and Sm-Nd isotopic constraints on crustal growth and emplacement. *Journal of Geophysical Research: Solid Earth* 2013, **118**(5)**:** 2085-2101.

17. Reagan MK, Heaton DE, Schmitz MD, Pearce JA, Shervais JW, Koppers AAP. Forearc ages reveal extensive short-lived and rapid seafloor spreading following subduction initiation. *Earth and Planetary Science Letters* 2019, **506:** 520-529.

18. Ishizuka O, Tani K, Reagan MK, Kanayama K, Umino S, Harigane Y*, et al.* The timescales of subduction initiation and subsequent evolution of an oceanic island arc. *Earth and Planetary Science Letters* 2011, **306**(3)**:** 229-240.

19. Arculus RJ, Ishizuka O, Bogus KA, Gurnis M, Hickey-Vargas R, Aljahdali MH*, et al.* A record of spontaneous subduction initiation in the Izu–Bonin–Mariana arc. *Nature Geoscience* 2015, **8**(9)**:** 728-733.

20. Soret M, Bonnet G, Agard P, Larson KP, Cottle JM, Dubacq B*, et al.* Timescales of subduction initiation and evolution of subduction thermal regimes. *Earth and Planetary Science Letters* 2022, **584:** 117521.

21. Roberts NMW, Thomas RJ, Jacobs J. Geochronological constraints on the metamorphic sole of the Semail ophiolite in the United Arab Emirates. *Geoscience Frontiers* 2016, **7**(4)**:** 609-619.

22. Hacker BR, Mosenfelder JL. Metamorphism and deformation along the emplacement thrust of the Samail ophiolite, Oman. *Earth and Planetary Science Letters* 1996, **144**(3-4)**:** 435-451.

23. Hacker BR, Mosenfelder JL, Gnos E. Rapid emplacement of the Oman ophiolite: Thermal and geochronologic constraints. *Tectonics* 1996, **15**(6)**:** 1230-1247.

24. Searle M, Rioux M, Garber JM. One line on the map: A review of the geological history of the Semail Thrust, Oman-UAE mountains. *Journal of Structural Geology* 2022, **158:** 104594.

25. Garber JM, Rioux M, Kylander-Clark ARC, Hacker BR, Vervoort JD, Searle MP. Petrochronology of Wadi Tayin Metamorphic Sole Metasediment, With Implications for the Thermal and Tectonic Evolution of the Samail Ophiolite (Oman/UAE). *Tectonics* 2020, **39**(12)**:** e2020TC006135.

26. Ishikawa T, Fujisawa S, Nagaishi K, Masuda T. Trace element characteristics of the fluid liberated from amphibolite-facies slab: Inference from the metamorphic sole beneath the Oman ophiolite and implication for boninite genesis. *Earth and Planetary Science Letters* 2005, **240**(2)**:** 355-377.

27. Ambrose TK, Waters DJ, Searle MP, Gopon P, Forshaw JB. Burial, Accretion, and Exhumation of the Metamorphic Sole of the Oman-UAE Ophiolite. *Tectonics* 2021, **40**(4)**:** e2020TC006392.

28. Gnos E. Peak Metamorphic Conditions of Garnet Amphibolites Beneath the Semail Ophiolite: Implications for an Inverted Pressure Gradient. *International Geology Review* 1998, **40**(4)**:** 281-304.

29. Soret M, Agard P, Ildefonse B, Dubacq B, Prigent C, Rosenberg C. Deformation mechanisms in mafic amphibolites and granulites: record from the Semail metamorphic sole during subduction infancy. *Solid Earth* 2019, **10**(5)**:** 1733-1755.

30. Cowan RJ, Searle MP, Waters DJ. Structure of the metamorphic sole to the Oman Ophiolite, Sumeini Window and Wadi Tayyin: implications for ophiolite obduction processes. *Geological Society, London, Special Publications* 2014, **392**(1)**:** 155-175.

31. Krogh EJ. The garnet-clinopyroxene Fe-Mg geothermometer — a reinterpretation of existing experimental data. *Contributions to Mineralogy and Petrology* 1988, **99**(1)**:** 44-48.

32. Ravna K. The garnet–clinopyroxene Fe2+–Mg geothermometer: an updated calibration. *Journal of Metamorphic Geology* 2000, **18**(2)**:** 211-219.

33. Sun C, Liang Y. A REE-in-garnet–clinopyroxene thermobarometer for eclogites, granulites and garnet peridotites. *Chemical Geology* 2015, **393–394:** 79-92.

34. Pickles JR, Blundy JD, Brooker RA. Trace element thermometry of garnet-clinopyroxene pairs. *American Mineralogist* 2016, **101**(6)**:** 1438-1450.

35. Caddick MJ, Konopásek J, Thompson AB. Preservation of Garnet Growth Zoning and the Duration of Prograde Metamorphism. *Journal of Petrology* 2010, **51**(11)**:** 2327-2347.

36. Wu L-G, Li Y, Jollands MC, Vermeesch P, Li X-H. Diffuser: A user-friendly program for diffusion chronometry with robust uncertainty estimation. *Computers & Geosciences* 2022, **163:** 105108.

37. Carlson WD. Rates of Fe, Mg, Mn, and Ca diffusion in garnet. *American Mineralogist* 2006, **91**(1)**:** 1-11.

38. Chakraborty S, Ganguly J. Cation diffusion in aluminosilicate garnets: experimental determination in spessartine-almandine diffusion couples, evaluation of effective binary diffusion coefficients, and applications. *Contributions to Mineralogy and Petrology* 1992, **111**(1)**:** 74-86.

39. Vielzeuf D, Baronnet A, Perchuk AL, Laporte D, Baker MB. Calcium diffusivity in alumino-silicate garnets: an experimental and ATEM study. *Contributions to Mineralogy and Petrology* 2007, **154**(2)**:** 153-170.

40. Chu X, Ague JJ. Analysis of experimental data on divalent cation diffusion kinetics in aluminosilicate garnets with application to timescales of peak Barrovian metamorphism, Scotland. *Contributions to Mineralogy and Petrology* 2015, **170**(2)**:** 25.

41. Bloch EM, Jollands MC, Devoir A, Bouvier A-S, Ibañez-Mejia M, Baumgartner LP. Multispecies diffusion of yttrium, rare earth elements and hafnium in garnet. *Journal of Petrology* 2020.

42. Cherniak DJ. Yb and Y diffusion in grossular garnet. *Geochemica et Cosmochimica Acta* 2005, **69 (suppl.):** 405.

43. Carlson WD. Rates and mechanism of Y, REE, and Cr diffusion in garnet. *American Mineralogist* 2012, **97**(10)**:** 1598-1618.

44. Ague JJ, Baxter EF. Brief thermal pulses during mountain building recorded by Sr diffusion in apatite and multicomponent diffusion in garnet. *Earth and Planetary Science Letters* 2007, **261**(3)**:** 500-516.

45. Konrad-Schmolke M, Halama R, Chew D, Heuzé C, De Hoog J, Ditterova H. Discrimination of thermodynamic and kinetic contributions to the heavy rare earth element patterns in metamorphic garnet. *Journal of Metamorphic Geology* 2023, **41**(4)**:** 465-490.

46. Kotowski AJ, Cloos M, Stockli DF, Bos Orent E. Structural and Thermal Evolution of an Infant Subduction Shear Zone: Insights From Sub-Ophiolite Metamorphic Rocks Recovered From Oman Drilling Project Site BT-1B. *Journal of Geophysical Research: Solid Earth* 2021, **126**(12)**:** e2021JB021702.

47. England PC, Smye AJ. Metamorphism and Deformation on Subduction Interfaces: 1. Physical Framework. *Geochemistry, Geophysics, Geosystems* 2023, **24**(1)**:** e2022GC010644.

48. Duprat-Oualid S, Yamato P, Schmalholz SM. A dimensional analysis to quantify the thermal budget around lithospheric-scale shear zones. *Terra Nova* 2015, **27**(3)**:** 163-168.

49. Agard P, Prigent C, Soret M, Dubacq B, Guillot S, Deldicque D. Slabitization: Mechanisms controlling subduction development and viscous coupling. *Earth-Science Reviews* 2020**:** 103259.

METHODS

Electron probe microanalysis (EPMA). Garnet major-element compositional maps and spot transects for samples 13OJGWT15 and 171213J02 were collected using a Cameca SX-5 electron microprobe at the Materials Characterization Laboratory, Penn State. All samples were analyzed in thin section. Natural and synthetic mineral samples were used as reference materials. Garnet X-ray maps (Al, Ca, Cr, Fe, K, Mg, Mn, Na, Si, Ti) were acquired on the SX-5 with an accelerating voltage of 25 kV, a beam current of 20 nA, a focused beam, a 512x512 pixel resolution, and a step size of 7 µm (13OJGWT15) or 8 µm (171213J02). Locations for quantitative garnet traverses were selected from X-ray maps. Quantitative garnet, clinopyroxene, hornblende, and plagioclase feldspar data were collected for the same 10 elements with an accelerating voltage of 20 kV, a beam current of 20 nA, and a focused beam. Spots with low (<98.5%) or high totals (>101.0%) were culled from the dataset. The garnet map and quantitative spot data were processed in XMapTools version 3.4[50] to yield quantified garnet major-element maps. The quantitative data used for map calibration were also used for garnet-clinopyroxene Fe-Mg thermometry (**Fig. S3**). Transect data for major-element diffusion modelling (**Fig. 3**; **Fig. S4**) are shown in **Table S2**; these data were collected along a quantitative EPMA spot transect, but profiles extracted from both EPMA and LAICPMS maps along the same line yield identical values within uncertainty. The full suite of major-element maps is contained in **Figs. S6-S7**. Garnet and clinopyroxene compositions for Fe-Mg thermometry are shown in **Table S3**.

Laser-ablation inductively coupled plasma mass spectrometry (LA-ICPMS) mapping. The same garnet grains mapped by EPMA were subsequently mapped using LA-ICPMS at the University of Maine MicroAnalytical Geochemistry and Isotope Characterization (MAGIC) Laboratory. The analytical setup consisted of an ESI NWR193^{UC} laser ablation system equipped with a TV2 large format cell, coupled to an Agilent 8900 ICPMS. The mapping setup consisted of an ESI dual concentric injector (DCI1) ICP-MS torch and 1mm ID tubing connected directly from the laser cell to the DCI. The laser ablation aerosol was transported using He as a carrier gas with a flow rate of 1 L/min.

Maps were acquired using a 6 x 6 μm square spot rastered across the sample surface with a scan speed of 1300 μm s^{-1}, beam energy density of ~4 J/cm^2, and a repetition rate of 150 Hz. Peaks were measured at ^{24}Mg, ^{27}Al, ^{44}Ca, ^{52}Cr, ^{89}Y, ^{163}Dy, and ^{175}Lu for both maps, with the addition of ^{45}Sc for 171213J02. Time-resolved signals were processed using the Trace Elements DRS in iolite 4. USGS basalt glass GSE-1G was used as a primary calibration material. Basalt glass GSD-1G was run as a quality control material; measured values agree within 5% of their GeoREM preferred values for all elements except Cr, which is within 10%. Mass fractions in garnet were determined by applying 11.75 weight % Al as an internal standard element (consistent with the EPMA data from the same garnets). Trace element maps were produced using CellSpace in iolite v4[51-53]; quantitative trace-element transects (**Fig. 4**; **Tables S4-S6**) were extracted from these maps for use in diffusion modelling.

Additional spot data were collected at the Penn State LionChron facility on other granulite-facies garnet and clinopyroxene rims from both samples for use in REE thermometry[33]. Samples were ablated in thin section using a Teledyne/Photon Machines Analyte G2 excimer laser ablation system with a Helex2 ablation cell, coupled to a Thermo Scientific iCAP-RQ ICPMS system for trace elements. The total Ar gas flow for the experiment was ~1 L/min, with total He gas flows from the laser at 0.44 L/min. All samples were run during the same session, with a 40 μm spot, 10 Hz repetition rate, 200 shots, and a laser fluence at the sample surface of ~3.05 J/cm^2. The laser was first fired thrice with the same spot size to remove surface contamination, and this material was allowed to wash out for 15 s. Analyses of unknowns were bracketed by analyses of NIST SRM 612 glass[54] and whole-rock glasses from the Max-Planck-Institut[55], including Gorgona Island komatiite G128-G, Kilauea basalt KL2-G, Mauna Loa basalt ML3B-G, Alpine quartz diorite T1-G, and Mt. St. Helens andesite StHs6/80-G. KL2-G was used as the primary reference material for all analyses. For trace-element quantification, ^{29}Si (assuming 17.5 wt. % Si, consistent with the EPMA data) was used as an internal standard, with measured peaks on the iCAP-RQ at ^{23}Na, ^{24}Mg, ^{27}Al, ^{29}Si, ^{31}P, ^{43}Ca, ^{45}Sc, ^{49}Ti, ^{51}V, ^{52}Cr, ^{55}Mn, ^{57}Fe, ^{59}Co, ^{60}Ni, ^{63}Cu, ^{66}Zn, ^{88}Sr, ^{89}Y, ^{90}Zr, ^{93}Nb, ^{95}Mo, ^{137}Ba, ^{139}La, ^{140}Ce, ^{141}Pr, ^{146}Nd, ^{147}Sm, ^{153}Eu, ^{157}Gd, ^{159}Tb, ^{163}Dy, ^{165}Ho, ^{166}Er, ^{169}Tm, ^{172}Yb, ^{175}Lu, ^{180}Hf, ^{181}Ta, and ^{182}W. Iolite version 4[52] was used to corrected measured elemental intensities for baselines and instrumental drift. Using the same methods as applied to unknowns, and treating all whole-rock glasses besides KL2-G as secondary reference materials, this routine yielded REE values accurate to ≤5%. The REE data used for thermometry are shown in **Table S7.**

Major and trace-element diffusion speedometry. Characteristic timescales of peak metamorphism were estimated by forward modeling of major element diffusion through garnet. Measured concentration profiles (e.g., Fig. S4) were compared to those calculated for radial, multicomponent diffusion in a sphere for three independent (Fe, Mg, Mn) and one dependent

(Ca) components[56]. Our modeling approach broadly follows that of ref. [35]. We used an explicit finite difference scheme to solve an expanded version of Fick's second law:

$$\frac{\partial X}{\partial t} = \frac{1}{r^2}\frac{\partial}{\partial r}\left[r^2 D\frac{\partial X}{\partial r}\right] \qquad \text{(Eq. S1)}$$

in which X is a vector of garnet mole fractions, t is time, D is a matrix of interdependent diffusion coefficients and r is radial coordinate. Garnet composition was initially specified either side of an imposed step function located at the center of each concentration profile. Elements of the diffusion coefficient matrix were calculated at each time step using the following expression for ionic solutions[57]:

$$D_{ij} = D_i^*\delta_{ij} - \left[\frac{D_i^* X_i}{\sum_{k=1}^{4} D_k^* X_k}\right]\left(D_j^* - D_{Ca}^*\right) \qquad \text{(Eq. S2)}$$

in which $D_{i,j,Ca}^*$ are cation tracer diffusivities and δ_{ij} is Kronecker's delta. We used the model of Carlson 2006[37] to calculate tracer diffusion coefficients, which are a function of unit cell dimensions, pressure and oxygen fugacity:

$$lnD_i^* = D_{0,i}^* + \Delta\alpha_{0,i} - \frac{Q_i + P\Delta V_i}{RT} + \frac{1}{6}ln\left(\frac{f_{O2}}{f_{O2}^{graphite}}\right) \qquad \text{(Eq. S3)}$$

in which Q_i is molar activation energy, V_i is molar volume, $\Delta\alpha_{0,i}$ is the scaled product of the difference in unit cell size between end-member i and the garnet composition[37]. All calculations were performed at 10 kbar and with $\frac{f_{O2}}{f_{O2}^{graphite}} = 1$ (i.e. at graphite–oxygen equilibrium). Time step (Δt) size was calculated using the Fourier mesh number (F) to ensure numerical stability:

$$F \equiv \frac{D\Delta t}{(\Delta r)^2} \qquad \text{(Eq. S4)}$$

We used three sets of garnet diffusion parameters to calculate major element concentration profiles: (1) the empirically-derived values from ref. 40 (left-hand column, Fig. S4), (2) Mn, Mg and Fe parameters from ref. 41 combined with Ca parameters from ref. 42 (central column, Fig. S4), and (3) the statistically-derived parameter set from ref. 43 (right-hand column, Fig. S4).

Trace-element (Lu) speedometry was performed using analytical solutions to the diffusion equation, using the online version of the Diffuser software[36] for MATLAB. The inverted profiles are shown in **Fig. 4d-f** and contained in **Tables S3-S4**; the full range of results is contained in **Fig. S5**. In each case, a step function was assumed as the initial case and modeled with multiple combinations of peak temperature (700-800°C) and published garnet diffusion parameters from multiple sources[41-43]. We tested three sets of experimentally determined Lu-in-garnet diffusion parameters: **i**) a "fast" endmember[41] most appropriate for the low Lu concentrations in our dataset; **ii**) a "slow" endmember[41], which is theoretically appropriate only for elevated (>500 ppm) REE concentrations; and **iii**) a suite of intermediate diffusivities[42, 43]. Because the slowest garnet REE diffusion mechanism is pressure-sensitive[41], its Ea was corrected to 1 GPa for all modelling, consistent with previously published metamorphic pressure data from the Samail metamorphic soles analyzed in this study (**Fig. S3**).

Lutetium-hafnium (Lu-Hf) garnet dating. Four ≤250 mg garnet separates were extracted from sample 17123J02 using standard mineral separation techniques (excluding heavy liquids) at Penn State. Whole-rock powders were generated from several ~2–4-cm sized rock fragments using alumina crushing equipment and ceramic-lined grinding containers in a SPEX mixer mill at Franklin and Marshall University. Chemical dissolution, ion-exchange chromatography, and radiogenic isotope measurements were performed at the Radiogenic Isotope and Geochronology Laboratory at Washington State University using a Neptune Plus MC-ICP-MS, using the methods outlined in ref. [58]. All isochron calculations were performed using Isoplot[59] and checked for consistency in IsoplotR[60] with $\lambda_{Lu} = 1.867 \times 10^{-11}$ yr^{-1} (ref. [61]). εHf was calculated using chondritic uniform reservoir (CHUR) parameters from ref. [62] (^{176}Hf/^{177}Hf$_{CHUR}$ = 0.282785 ± 0.000011, ^{176}Lu/^{177}Hf$_{CHUR}$ = 0.0336 ± 0.0001). Previously published zircon Lu-Hf isotopic data for the same sample[14] were also included and compared to the solution data. The final Lu-Hf data, calculated date(s), and εHf are shown in Table S1.

Data Availability Statement

All data supporting the conclusions in this study (Tables S1-S7) are freely available online at doi:10.17605/OSF.IO/ZNT7S (ref. [63]).

METHODS-ONLY REFERENCES

50. Lanari P, Vidal O, De Andrade V, Dubacq B, Lewin E, Grosch EG, Schwartz S. XMapTools: A MATLAB©-based program for electron microprobe X-ray image processing and geothermobarometry. *Computers & Geosciences* 2014, **62:** 227-240.

51. Woodhead JD, Hellstrom J, Hergt JM, Greig A, Maas R. Isotopic and Elemental Imaging of Geological Materials by Laser Ablation Inductively Coupled Plasma-Mass Spectrometry. *Geostandards and Geoanalytical Research* 2007, **31**(4)**:** 331-343.

52. Paton C, Hellstrom J, Paul B, Woodhead J, Hergt J. Iolite: Freeware for the visualisation and processing of mass spectrometric data. *Journal of Analytical Atomic Spectrometry* 2011, **26**(12)**:** 2508-2518.

53. Paul B, Paton C, Norris A, Woodhead J, Hellstrom J, Hergt J, Greig A. CellSpace: A module for creating spatially registered laser ablation images within the Iolite freeware environment. *Journal of Analytical Atomic Spectrometry* 2012, **27**(4)**:** 700-706.

54. Pearce NJG, Perkins WT, Westgate JA, Gorton MP, Jackson SE, Neal CR, Chenery SP. A Compilation of New and Published Major and Trace Element Data for NIST SRM 610 and NIST SRM 612 Glass Reference Materials. *Geostandards Newsletter* 1997, **21**(1)**:** 115-144.

55. Jochum KP, Stoll B, Herwig K, Willbold M, Hofmann AW, Amini M*, et al.* MPI-DING reference glasses for in situ microanalysis: New reference values for element concentrations and isotope ratios. *Geochemistry, Geophysics, Geosystems* 2006, **7**(2).

56. Onsager L. Theories and problems of liquid diffusion. *Annals of the New York Academy of Sciences* 1945, **46**(5)**:** 241-265.

57. Lasaga AC. Multicomponent exchange and diffusion in silicates. *Geochimica et Cosmochimica Acta* 1979, **43**(4)**:** 455-469.

58. Johnson TA, Vervoort JD, Ramsey MJ, Aleinikoff JN, Southworth S. Constraints on the timing and duration of orogenic events by combined Lu–Hf and Sm–Nd geochronology: An example from the Grenville orogeny. *Earth and Planetary Science Letters* 2018, **501:** 152-164.

59. Ludwig KR. *Isoplot 3.00: A Geochronological Toolkit for Microsoft Excel*. Berkeley Geochronology Center Special Publication, 2003.

60. Vermeesch P. IsoplotR: A free and open toolbox for geochronology. *Geoscience Frontiers* 2018, **9**(5)**:** 1479-1493.

61. Söderlund U, Patchett PJ, Vervoort JD, Isachsen CE. The 176Lu decay constant determined by Lu–Hf and U–Pb isotope systematics of Precambrian mafic intrusions. *Earth and Planetary Science Letters* 2004, **219**(3–4)**:** 311-324.

62. Bouvier A, Vervoort JD, Patchett PJ. The Lu–Hf and Sm–Nd isotopic composition of CHUR: Constraints from unequilibrated chondrites and implications for the bulk composition of terrestrial planets. *Earth and Planetary Science Letters* 2008, **273**(1)**:** 48-57.

63. Garber, J.M., et al., Shear heating during rapid subduction initiation beneath the Samail Ophiolite. *Open Science Framework* doi:10.17605/OSF.IO/ZNT7S, 2025.

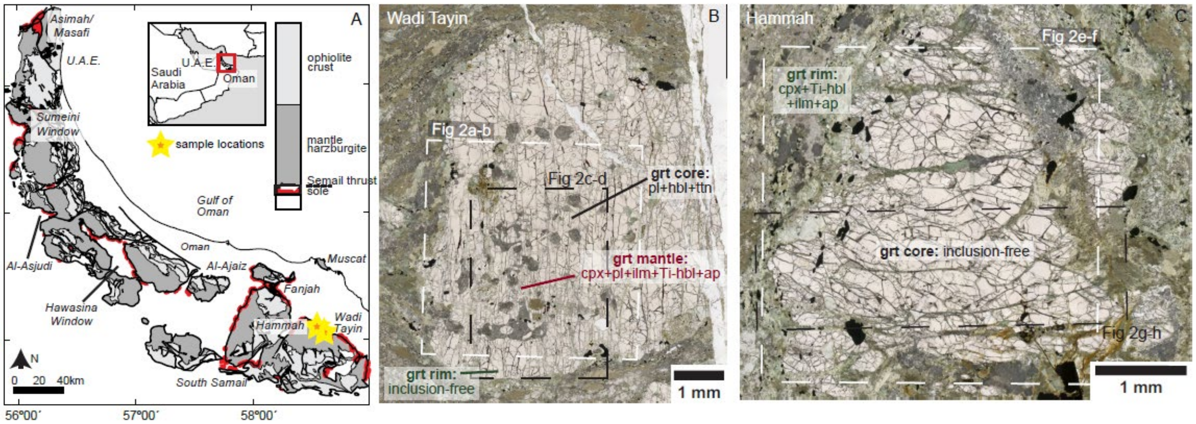
A
Asimah/ Masafi
U.A.E.
Sumeini Window
Al-Asjudi
Hawasina Window
Gulf of Oman
Oman
Al-Ajaiz
Muscat
Fanjah
Hammah
Wadi Tayin
South Samail
U.A.E.
Saudi Arabia
Oman
sample locations
ophiolite crust
mantle harzburgite
Semail thrust
sole
N
0 20 40km
25°00'
24°00'
23°00'
56°00'
57°00'
58°00'
Wadi Tayin
B
Fig 2a-b
Fig 2c-d
grt core: pl+hbl+ttn
grt mantle: cpx+pl+ilm+Ti-hbl+ap
grt rim: inclusion-free
1 mm
Hammah
C
Fig 2e-f
grt rim: cpx+Ti-hbl +ilm+ap
grt core: inclusion-free
Fig 2g-h
1 mm

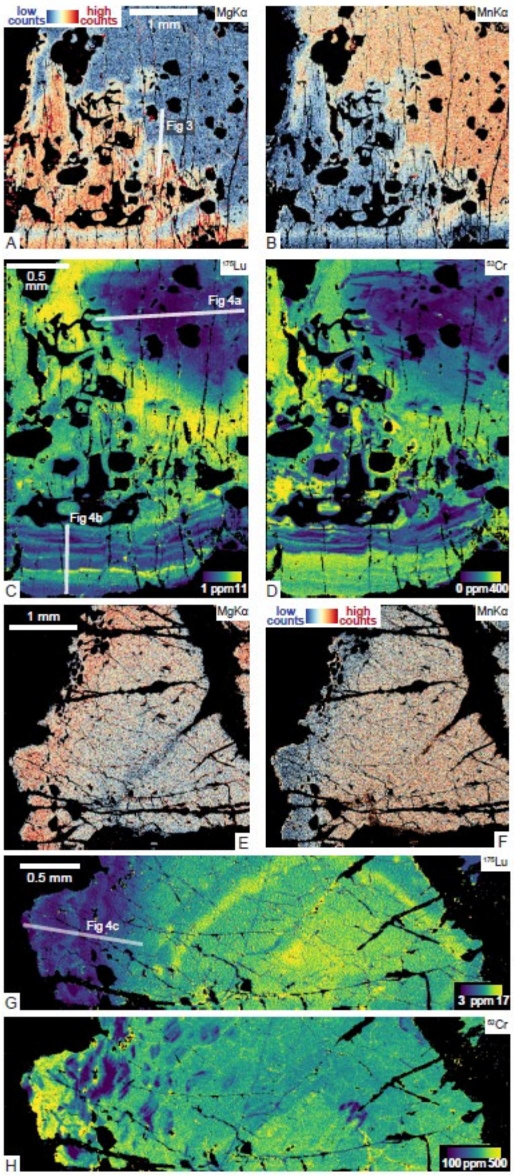
low counts
high counts
1 mm
MgKα
MnKα
Fig 3
A
B
0.5 mm
175Lu
53Cr
Fig 4a
Fig 4b
1 ppm 11
0 ppm 400
C
D
1 mm
MgKα
low counts
high counts
MnKα
E
F
0.5 mm
175Lu
Fig 4c
3 ppm 17
G
53Cr
100 ppm 500
H

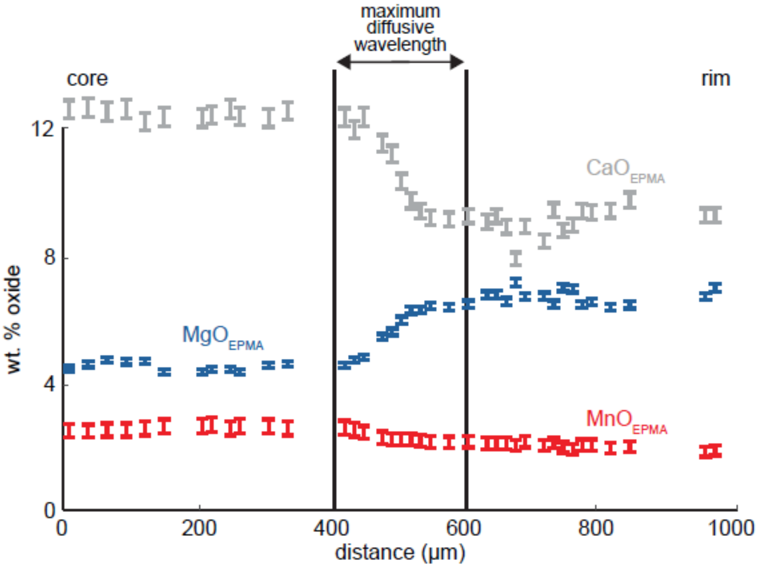
maximum
diffusive
wavelength
core
rim
CaO$_{EPMA}$
MgO$_{EPMA}$
MnO$_{EPMA}$
wt. % oxide
12
8
4
0
0
200
400
600
800
1000
distance (μm)

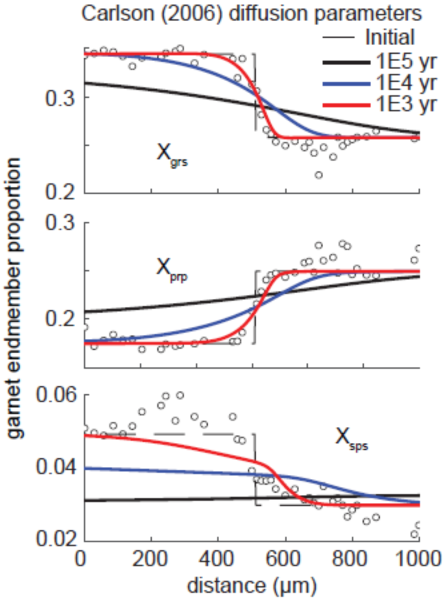
Carlson (2006) diffusion parameters
Initial
1E5 yr
1E4 yr
1E3 yr
X_{grs}
X_{prp}
X_{sps}
garnet endmember proportion
0.3
0.2
0.3
0.2
0.06
0.04
0.02
0
200
400
600
800
1000
distance (μm)

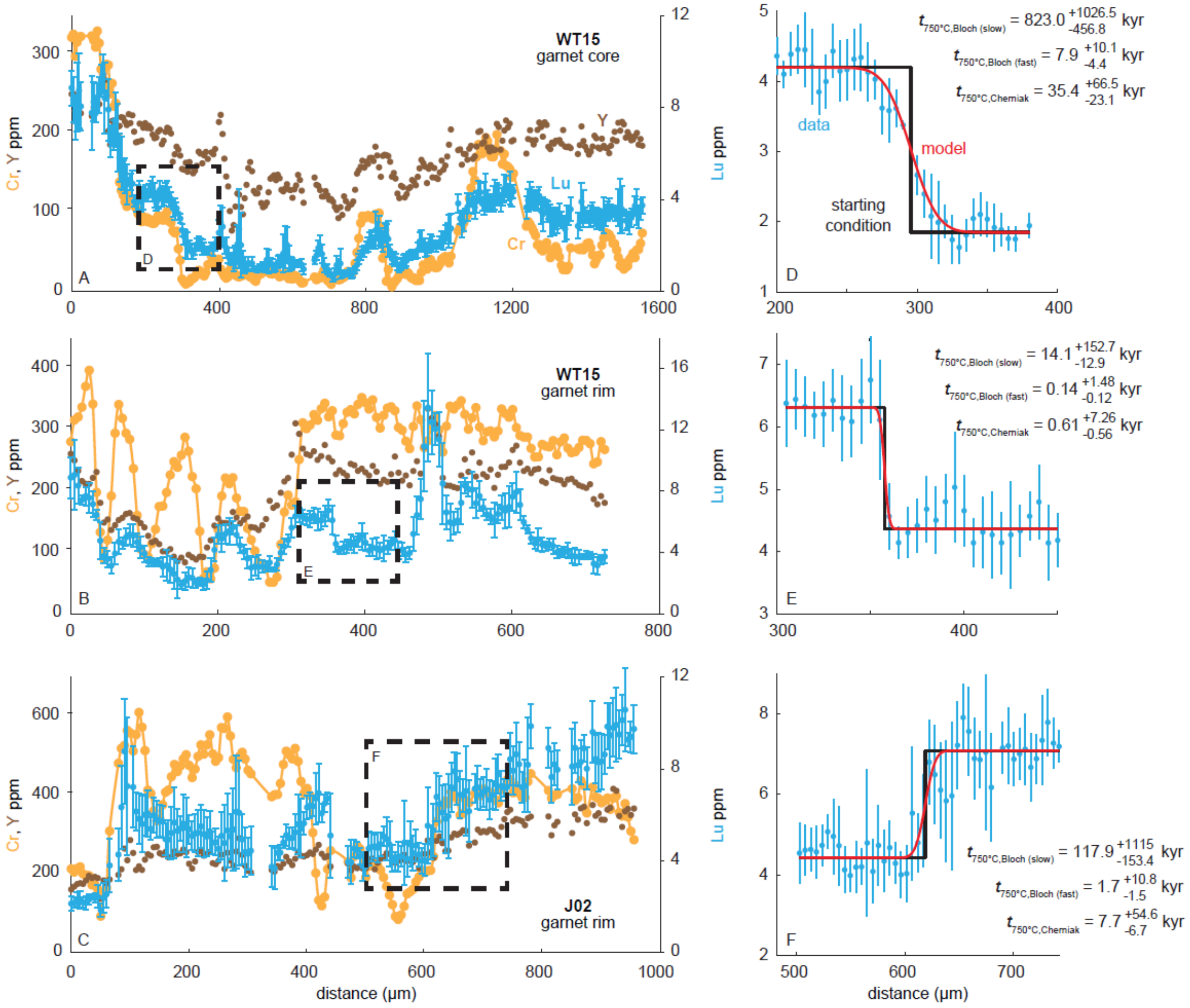

WT15
garnet core
Y
Lu
Cr
D
A
Cr, Y ppm
Lu ppm
0
100
200
300
0
4
8
12
0
400
800
1200
1600
$t_{750°C,Bloch (slow)}$ = 823.0 $^{+1026.5}_{-456.8}$ kyr
$t_{750°C,Bloch (fast)}$ = 7.9 $^{+10.1}_{-4.4}$ kyr
$t_{750°C,Cherniak}$ = 35.4 $^{+66.5}_{-23.1}$ kyr
data
model
starting condition
D
1
2
3
4
5
200
300
400
WT15
garnet rim
E
B
0
100
200
300
400
0
4
8
12
16
0
200
400
600
800
$t_{750°C,Bloch (slow)}$ = 14.1 $^{+152.7}_{-12.9}$ kyr
$t_{750°C,Bloch (fast)}$ = 0.14 $^{+1.48}_{-0.12}$ kyr
$t_{750°C,Cherniak}$ = 0.61 $^{+7.26}_{-0.56}$ kyr
E
3
4
5
6
7
300
400
J02
garnet rim
F
C
0
200
400
600
0
4
8
12
0
200
400
600
800
1000
distance (µm)
$t_{750°C,Bloch (slow)}$ = 117.9 $^{+1115}_{-153.4}$ kyr
$t_{750°C,Bloch (fast)}$ = 1.7 $^{+10.8}_{-1.5}$ kyr
$t_{750°C,Cherniak}$ = 7.7 $^{+54.6}_{-6.7}$ kyr
F
2
4
6
8
500
600
700
distance (µm)

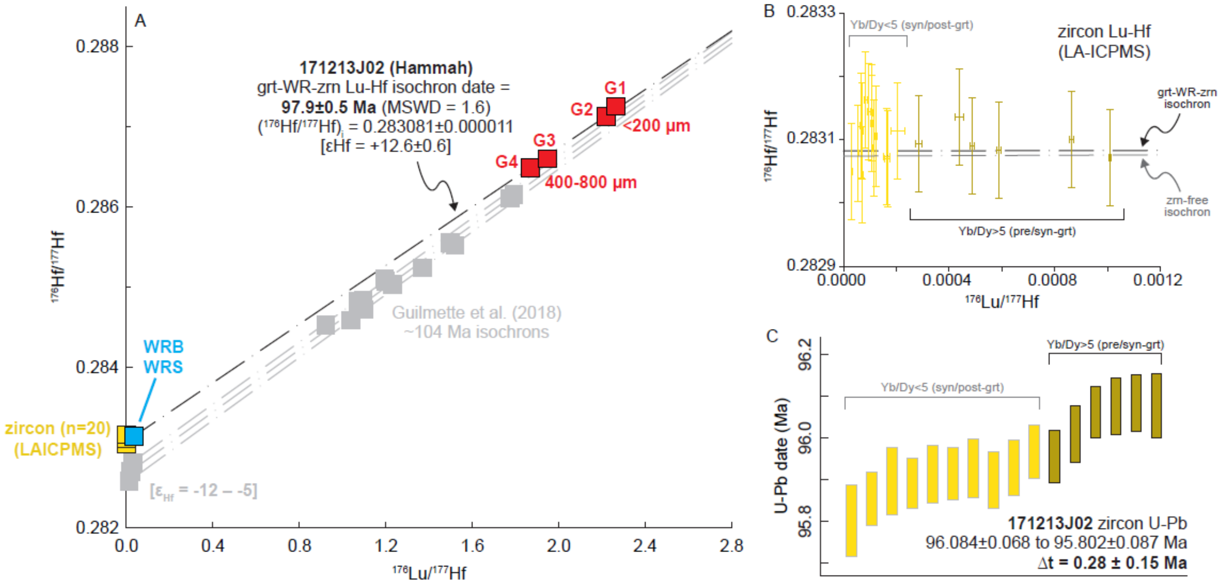
A
0.288
0.286
0.284
0.282
^{176}Hf/^{177}Hf
0.0
0.4
0.8
1.2
1.6
2.0
2.4
2.8
^{176}Lu/^{177}Hf
171213J02 (Hammah)
grt-WR-zrn Lu-Hf isochron date =
97.9±0.5 Ma (MSWD = 1.6)
(^{176}Hf/^{177}Hf)$_i$ = 0.283081±0.000011
[εHf = +12.6±0.6]
G1
G2
<200 μm
G3
G4
400-800 μm
Guilmette et al. (2018)
~104 Ma isochrons
WRB
WRS
zircon (n=20)
(LAICPMS)
[ε$_{Hf}$ = -12 – -5]
B
0.2833
0.2831
0.2829
^{176}Hf/^{177}Hf
Yb/Dy<5 (syn/post-grt)
zircon Lu-Hf
(LA-ICPMS)
grt-WR-zrn isochron
zrn-free isochron
Yb/Dy>5 (pre/syn-grt)
0.0000
0.0004
0.0008
0.0012
^{176}Lu/^{177}Hf
C
96.2
96.0
95.8
U-Pb date (Ma)
Yb/Dy>5 (pre/syn-grt)
Yb/Dy<5 (syn/post-grt)
171213J02 zircon U-Pb
96.084±0.068 to 95.802±0.087 Ma
Δt = 0.28 ± 0.15 Ma

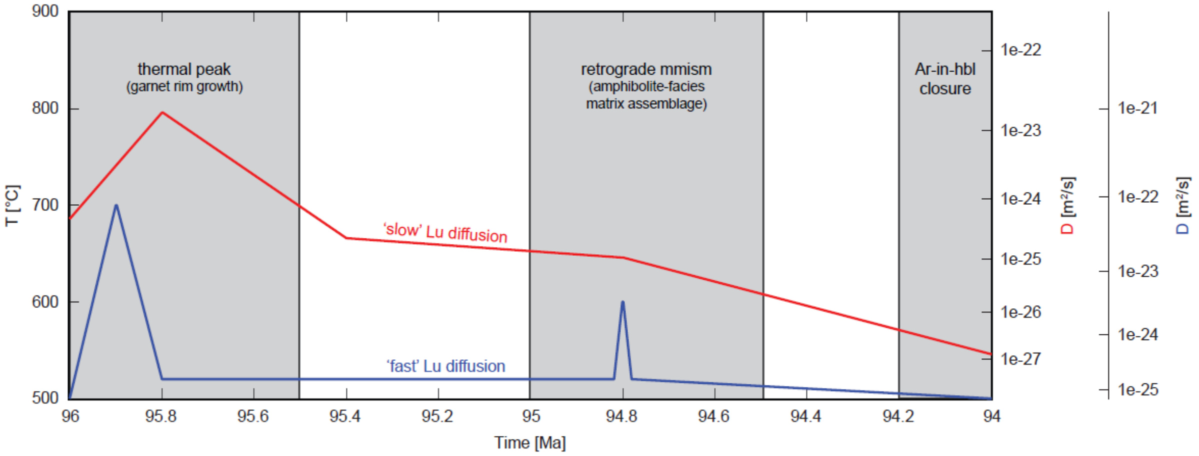
thermal peak
(garnet rim growth)
retrograde mmism
(amphibolite-facies
matrix assemblage)
Ar-in-hbl
closure
'slow' Lu diffusion
'fast' Lu diffusion
T [°C]
900
800
700
600
500
96
95.8
95.6
95.4
95.2
95
94.8
94.6
94.4
94.2
94
Time [Ma]
1e-22
1e-23
1e-24
1e-25
1e-26
1e-27
D [m²/s]
1e-21
1e-22
1e-23
1e-24
1e-25
D [m²/s]